Biodegradable Metal–Organic Framework-Based Microrobots (MOFBOTs)

Originally published in:
Advanced Healthcare Materials 9(20), https://doi.org/10.1002/adhm.202001031

Funding acknowledgement:
ETH-33 17-1 - MOFBOTS: Supramolecular-based highly integrated soft robots (ETHZ)
181988 - Functional 2D porous crystalline materials (2DMats) (SNF)
677020 - Microfluidic Crystal Factories (μ-CrysFact): a breakthrough approach for crystal engineering (EC)

Biodegradable Metal-organic Framework based Microrobots (MOFBOTs)

Anastasia Terzopoulou, Xiaopu Wang, Xiang-Zhong Chen, Mario Palacios-Corella, Carlos Pujante, Javier Herrero-Martín, Dr. Xiao-Hua Qin, Jordi Sort, Andrew J. deMello, Bradley J. Nelson, Josep Puigmartí-Luis*, and Salvador Pané*

A. Terzopoulou, X. Wang, Dr. X.-Z. Chen, Prof. B. J. Nelson, Prof. S. Pané
Institute of Robotics and Intelligent Systems, ETH Zurich
Tannenstrasse 3, CH-8092 Zurich, Switzerland
Email: chenxian@ethz.ch

C. Pujante, Prof. A. J. de Mello, Dr. J. Puigmartí-Lui
Institute for Chemical and Bioengineering, ETH Zurich
Tannenstrasse 3, CH-8092 Zurich, Switzerland
E-mail: josep.puigmarti@chem.ethz.ch

M. Palacios-Corella
Instituto de Ciencia Molecular, Universidad de Valencia,
Catedratico Jose Beltran 2, Paterna, 46980, Spain

Dr. J. Herrero-Martin
ALBA Synchrotron Light Source,
E-08290, Cerdanyola del Vallès, Barcelona, Spain

Dr. X.-H. Qin
Institute for Biomechanics, ETH Zurich
Leopold-Ruzicka-Weg 4, 8093 Zürich, Switzerland

Prof. Jordi Sort
Departament de Física, Universitat Autonoma de Barcelona,
E-08193 Cerdanyola del Valles, Spain

Keywords: MOFs, ZIFs, microrobots, biodegradation, drug delivery

Microrobots and metal-organic frameworks (MOFs) have been identified as promising carriers for drug delivery applications. While the clinical applications of microrobots are limited by their low drug loading efficiencies and the poor degradability of the materials used for their fabrication, MOFs lack motility and targeted drug delivery capabilities. The combination of these two fields marks the beginning of a new era, MOF-based small-scale robots (MOFBOTs) for biomedical applications. Yet, biodegradability is a major hurdle in the field of micro- and nanoswimmers including small-scale robots. Here, we report for the first time a highly integrated MOFBOT that is able to realize magnetic locomotion, drug delivery and selectively degrades in cell cultures. The MOF used in our investigations does not only allow a superior loading of chemotherapeutic drugs and their controlled release via a pH-responsive degradation but it also enables the controlled locomotion of enzymatically biodegradable gelatin-based helical microrobots under magnetic fields. The degradation of the integrated MOFBOT is observed after two weeks, when all its components fully degrade. Additionally, drug delivery studies performed in cancer cell cultures show reduced viability upon delivery of Doxorubicin within short time frames. This MOFBOT system opens new avenues for highly integrated fully biodegradable small-scale robots.

1. Introduction

The last two decades have seen the emergence of small-scale robots.[1] These tiny mobile devices hold great promise for a multitude of applications in the biomedical domain, particularly for targeted delivery of drugs and cells, sensing, diagnosis and microsurgery.[2] The main core of research activities in the field of small-scale robotics has focused on the locomotion aspect of these devices.[3] Researchers have thoroughly demonstrated the motile capabilities of micro- and nanorobots using different approaches such as the use of light, ultrasound, magnetic or electric fields, or combinations of these stimuli.[4] Currently, the community of small-scale roboticists is investigating new materials and fabrication schemes in order to fulfill all the features required for their translation into clinical applications.[5] Efforts directed at producing mobile micro- and nanorobots with enhanced biocompatibility, biodegradability and loading of therapeutic cargo have recently been reported.[6] Despite these advances, few examples of single small-scale robotic platforms exist that integrate all the necessary characteristics to become suitable candidates for realizing *in vivo* biomedical tasks.[7]

With the aim of realizing small-scale robots with both enhanced biocompatibility and biodegradability characteristics, we propose here a fully degradable hybrid system consisting of a soft polymeric chassis and a functional coating made of organomineralized magnetic metal-organic framework (MOF) composites.[8] MOFs are porous coordination polymers formed by metallic centers and organic linkers.[9] Their porous nature allows them to host therapeutic molecules.[10] Additionally, several MOFs, such as the zeolitic imidazolate framework -8 (ZIF-8), exhibit biodegradability and minimal cytotoxicity upon degradation,[11] making them ideal drug carriers with the capability of controlled release. However, MOFs lack motile features. There are several ways to provide MOFs with locomotion capabilities, such as catalytic propulsion, surface tension driven motion or magnetic navigation.[12] Compared to other motile

MOF systems, magnetic MOFs can be easily controlled by magnetic fields in terms of directionality of locomotion. Besides, magnetic fields are of particular interest in biomedical applications, since they can penetrate the body without causing damage to the tissues. In order to exploit magnetic fields to control the motion of MOFs, one strategy involves decorating magnetic micro- and/or nanostructures with MOF crystals. Various examples in the literature have shown the potential of this approach, however, the vast majority of these magnetic MOF composites suffer from either multi-step, complicated fabrication processes, or poor biocompatibility/biodegradability of the underlying components.[13] Additionally, their locomotion has only been demonstrated by dragging the MOF with permanent magnets.

Herein, a magnetic MOF composite synthesized with a single step synthetic protocol, i.e. Fe@ZIF-8, is used to achieve a highly integrated biocompatible and biodegradable MOFBOT (**Figure 1a**, and Supporting Information). Fe@ZIF-8 plays a dual role: i) it provides magnetic control over the locomotion of the MOFBOT and ii) it acts as an active delivery agent of therapeutic compounds. The chassis of the MOFBOT consist of biodegradable hydrogel microstructures made by direct-laser writing of gelatin methacryloyl (GelMA) for the chassis. We show that the integrated MOFBOT (Fe@ZIF-8@GelMA) can be guided under external magnetic fields, to perform drug delivery and ultimately degrade in a cell culture. The *in vitro* degradation process involves enzymatic degradation of the GelMA chassis and a pH-triggered degradation of Fe@ZIF-8 (Figure 1b).

2. Results and Discussion

2.1. Characterization of Fe@ZIF-8

We performed an extensive characterization of Fe@ZIF-8 and compared its compositional, morphological, structural and magnetic features with those of pristine ZIF-8. The morphology and elemental distribution of the particles were investigated with scanning electron microscopy (SEM) and energy dispersive X-ray spectroscopy (EDX), respectively. As shown in **Figure 2a**, while Fe@ZIF-8 crystals clearly have the typical dodecahedral shape of ZIF-8 **(Figure S1a)**, their size distribution is larger than ZIF-8 crystals with values of 900 ± 300 nm (Figure S1c-d). This variation in the particle size indicates that adding iron to the reaction media influences the crystallization mechanism, which results in a broader range of particle sizes.[8] Figure 2b shows the EDX elemental distribution maps of Fe@ZIF-8 crystals, which revealed the presence of C, N and Zn all over the framework as was expected. Additionally, and in sharp contrast to pristine ZIF-8 where Fe was not detected (Figure S1b), the EDX maps of Fe@ZIF-8 crystals also reveal a homogenous distribution of Fe. We then assessed if the porosity was preserved in Fe@ZIF-8 by means of Brunauer-Emmett-Teller (BET). N_2 absorption-desorption isotherms (Figure 2c) indicate a BET surface area of about 1500 m^2 g^{-1} for ZIF-8 and of 1200 m^2 g^{-1} for Fe@ZIF-8. Importantly, these values are in agreement with those previously reported for ZIF-8 crystals.[14] The smaller value of BET surface area found in Fe@ZIF-8 crystals is also consistent with the addition of iron(II) during its synthesis.[8] Figure 2d shows the magnetization curves of ZIF-8 and Fe@ZIF-8 powders obtained by vibrating sample magnetometry at room temperature. While ZIF-8 powders exhibit an expected weak diamagnetism, Fe@ZIF-8 crystals display a typical soft-ferro/ferrimagnetic behaviour with a saturation magnetization and a coercive field of 10 emu g^{-1} and 40 Oe, respectively. In order to investigate the origin of the magnetism observed in Fe@ZIF-8, we performed additional elementary analysis, X-ray diffraction (XRD) and X-ray absorption spectroscopy (XAS) measurements. We quantified the elemental content based on Rutherford Backscattering Spectroscopy (RBS) and Elastic Recoil Detection Analysis (ERDA). A detailed description of these measurements is provided in the supporting information. Compared to pure ZIF-8 in which the ratio of Zn, C, and N matches the chemical

formula, $C_8H_{10}N_4Zn$ **(Figure S2)**, Fe@ZIF-8 crystals show an excess amount of metal content with respect to the light elements, along with the presence of oxygen, suggesting the formation of metal oxides as a secondary phase in the system. This secondary phase present in Fe@ZIF-8 crystals could consist of iron oxides, zinc ferrites, or a mixture of these. The XRD patterns (Figure 2e) show that, while all the characteristic diffraction peaks of ZIF-8 can be observed in the pattern of Fe@ZIF-8, additional peaks (indicated with an asterisk *) are detected at 31.2º, 35.8º, 37.2º, 43.4º, 53.8º, 57.3º and 62.9º, representing possible spinel phases, such as magnetite, maghemite and zinc ferrite. To further investigate the nature of these oxides, we performed XAS and X-ray magnetic circular dichroism (XMCD) measurements across the Zn and Fe $L_{2,3}$ edges. All spectra were recorded at the BL29-BOREAS beamline of the ALBA Synchrotron (Barcelona, Spain) at room temperature under an applied magnetic field of 5 Tesla parallel to the propagation direction of the incident beam.[15] The signal detection mode was total electron yield. **Figure S3a** shows the similarity between the spectra recorded at the Zn $L_{2,3}$ edges for both Fe@ZIF-8 and the reference ZIF-8. All peaks identified for Fe@ZIF-8 are also present in the ZIF-8 system, indicating that the coordination of zinc is similar in both systems. Figure 2f shows the XAS and XMCD measurements at the Fe $L_{2,3}$ edges for Fe@ZIF-8. Indeed, we observed similarities to previously reported systems of zinc ferrite and maghemite.[16] The integral of the XMCD measurement (Figure 2f) tends to converge to zero, as expected, for a pure Fe^{3+} high spin-based system ($3d^5$ with t_{2g}^3 e_g^2 spins up configuration), denoting a quenched angular momentum. Interestingly, a weak but non-zero XMCD signal is evident in the Fe@ZIF-8 sample at the Zn $L_{2,3}$ edges (Figure S3b-c), indicating a partial occupation of Fe^{3+} sites by Zn cations in the sample. Based on these findings, we can conclude that a secondary phase of ferrite was formed *in situ* within the framework of Fe@ZIF-8. These ferrites are identified as zinc ferrite and maghemite, which explains the soft-magnetic properties of Fe@ZIF-8 crystals. Accordingly, Fe@ZIF-8 is a ferrimagnetic metal-organic framework composite.

2.2. Drug Delivery Capabilities of Fe@ZIF-8 particles

Prior to integrating Fe@ZIF-8 in a microrobotic platform, we first assessed the potential of Fe@ZIF-8 as a magnetically active biocompatible/biodegradable drug delivery system. Taking advantage of the pH-triggered degradability of ZIF-8-based systems,[11c] we specifically evaluated the release of the model anti-cancer drug Doxorubicin (DOX) loaded in Fe@ZIF-8 as a function of pH. **Figure 3a** shows the pH-responsive release of DOX from Fe@ZIF-8 particles in buffer solutions at acidic (pH=6, likewise a tumor extracellular environment) and at physiological (pH=7.4) conditions over 96 hours. As expected, a rapid release of DOX occurred in the acidic pH in the first 12 hours, with the complete drug release observed within 48 hours. In contrast, no drug release was observed with the physiological pH over a time period of 96 hours, suggesting that Fe@ZIF-8 can potentially maintain the therapeutic cargo at a physiological pH, and deliver it only in pathological acidic microenvironments (i.e.: pH=6) such as those encountered in the extracellular tumor matrix. Next, we performed *in-vitro* DOX delivery experiments to show the potential of Fe@ZIF-8 particles as drug delivery systems. Human breast cancer cells MDA-MB-231 were treated with both Fe@ZIF-8 and DOX@Fe@ZIF-8 particles. The LIVE/DEAD staining experiments in Figure 3b show that the cell population incubated with DOX@Fe@ZIF-8 resulted in aggregates of dead cells clearly marked in red. The treatment of cells with DOX-loaded Fe@ZIF-8 resulted in a reduced cell viability of about 35%. The cell viability (Figure 3c) was calculated using the control group, which did not undergo any treatment, as a reference (i.e. cells incubated with Fe@ZIF-8). After 72 hours the cell viability of the population treated with Fe@ZIF-8 remained at the highest levels (>90%), thus revealing that the killing efficiency of DOX@Fe@ZIF-8 was attributed to the released DOX and not to the Fe@ZIF-8 particles.

2.3 Degradability of Fe@ZIF-8 particles

As our ultimate goal is to develop a fully integrated and biodegradable microrobot, we next examined the impact of a cell culture environment in the Fe@ZIF-8 crystals. In relation to *in vivo* studies, which show that particle drug delivery systems tend to concentrate in the excretion organs[17], we investigated the outcome of Fe@ZIF-8 in human embryonic kidney (HEK) cells. Surprisingly, in these investigations we observed that after 2 days of incubation with Fe@ZIF-8 crystals, cells could be attracted with an external magnet, forming cell pellets from a suspension **(Figure S4)**. Confocal microscopy images presented in Figure 3d and **Figure S5** clearly show that the membrane of the cells in these studies were decorated with particles, which can be ascribed to the Fe@ZIF-8 crystals; this would explain the attraction of the cells to a magnet. Additionally, we further supported this hypothesis by monitoring the magnetic moment of the cell pellets at different times (Figure 3e). While at 0 hour the magnetic moment of the cell pellet had a value of $2.5 \cdot 10^{-3}$ emu, we observed that after 48 hours a decrease in the magnetic moment value was apparent. Indeed, at 120 hours, no net magnetic moment was measured in the cell pellet, indicating the degradation of the magnetic component in the composite. Moreover, the cell pellets also changed their color with time from dark brown – characteristic of the Fe@ZIF-8 particles – to light brown (Figure 3f). Accordingly, and based on these results, the Fe@ZIF-8 can be readily degraded in the cell culture over time. We also investigated the degradation products after 72 hours of incubation in terms of morphology and elementary distribution **(Figure S6)**. As expected, we could not find the typical Fe@ZIF-8 crystallites and only small particulates (most probably a mixture of metal oxides) with diameters less than 150 nm were present. Previous studies on ZIF-8 for biomedical applications suggest that the degradation mechanism of ZIF-8 involves the uptake of particles by cells and further hydrolysis in endosomes where the pH value is between 4.5 and 6.5.[18] Taking into account our results, a similar mechanism could be proposed for Fe@ZIF-8, where the degradation of the MOF framework (and the complete drug release) occurs over the time range

24 - 48 hours in acidic pH, and the magnetic phase degrades slowly (over 120 hours) in agreement with previous studies.[19]

2.4. Integration of Fe@ZIF-8 Particles as Microrobotic Architectures

Having demonstrated that Fe@ZIF-8 is a biocompatible and biodegradable magnetically active MOF, we next integrated Fe@ZIF-8 crystals onto the surface of 3D printed microchassis for controlled locomotion and drug delivery applications. In this work, GelMA was chosen as the biodegradable chassis, which led to the fabrication of a fully degradable and highly integrated microrobot system.[20] A helical shape was adopted, as it has been demonstrated to be favorable for the locomotion of small-scale robots in low Reynolds numbers at small scales.[21] As shown in **Figure 4a**, the integrated MOFBOTs (i.e. Fe@ZIF-8@GelMA) consist of Fe@ZIF-8 crystals decorating the GelMA microstructures. The dark contrast observed under the optical microscope clearly indicate the presence of the magnetic Fe@ZIF-8 crystals on the helical structures. Non-coated microstructures are transparent, with a light contrast created only on their edges **(Figure S7)**.

Magnetic manipulation of Fe@ZIF-8@GelMA was performed under rotating magnetic fields of 8 mT and at different frequencies. As shown in Figure 4b and in **Supplementary video 1**, at low frequencies (1-2 Hz), the Fe@ZIF-8@GelMA structures in contact with the substrate surface performed a rolling motion due to friction. At higher frequencies (e.g. 12 Hz), a corkscrew locomotion promoted the forward motion of the integrated MOFBOTs, see Figure 4c and **Supplementary video 2**. As the Fe@ZIF-8@GelMA structures were still partially in contact with the substrate surface, a lateral drift was still observed from the forward motion. Therefore, both rolling and corkscrew forward locomotions can be implemented for the transport of these integrated MOFBOTs.

In addition to the characterization of the motion performance, we conducted drug delivery experiments with Fe@ZIF-8@GelMA. The images in Figure 4d-e show cancer cells (MDA-

MB-231) incubated with the integrated MOFBOTs for 24 hours. As evident, cells incubated with Fe@ZIF-8@GelMA spread on the surface without signs of toxicity, whereas in the proximity of DOX@Fe@ZIF-8@GelMA most of the cells did not adhere to the surface, but floated as dead cells **(Figure S8)**. The degradation study of the integrated MOFBOTs in the cell culture over a longer period of time was also conducted (Figure 4f). In our experience, GelMA microrobots degrade faster in certain cell lines than others, a phenomenon related to the amount of proteases excreted by the cells. SH-SY5Y human neuroblastoma cells were chosen for MOFBOT degradation as we had previously observed quick degradation of the gels in this cell line. At day 0, we seeded the cells over the structures. The texture observed on the GelMA structures was attributed to the Fe@ZIF-8 crystals decorating their surface. After one week, we observed that crystals had detached from the surface of the GelMA structures. We also observed some floating agglomerates of gelatin degradation products, including Fe@ZIF-8 crystals. Further disassembly and degradation of those structures occurred by the end of the second week. The GelMA microstructures degraded in a cell culture by cell-secreted proteases. The exact mechanism involves proteolytic cleavage of the amide bonds of peptide domain in the GelMA, due to the action of proteolytic enzymes, such as collagenases and proteases excreted from various mammalian cell lines. Those enzymes act on the surface of the GelMA microstructures, resulting in the release of Fe@ZIF-8 crystals that decorate the surface, and eventually in the complete degradation of the MOFBOT chassis. As illustrated in Figure 4f, the helical integrated MOFBOTs appear to be degraded in the live cell culture on day 14. At the end of the degradation study, we performed a LIVE/DEAD staining to verify the viability of the cells in the culture. The fluorescent images presented in Figure 4g show an abundance of live cells in the culture. It is also evident that GelMA structures show fluorescence of a similar wavelength, therefore the non-degraded structures are green in the fluorescent image.

3. Conclusion

In this study, we introduced the first fully degradable magnetically maneuverable MOFBOT for drug delivery applications. The MOFBOT consists of a helical core made of biodegradable GelMA and a surface coating of Fe@ZIF-8, an organomineralized magnetic MOF composite. Fe@ZIF-8 preserves the advantages of ZIF-8, including high surface area and acidic pH responsiveness, features that make this MOF a desirable system for drug loading and spatiotemporal release. Additionally, the soft-magnetic properties of Fe@ZIF-8 provides magnetic motion capabilities under the guidance of external magnetic fields. Accordingly, the integrated MOFBOT can perform drug delivery tasks in a cell culture environment, resulting in reduced viability of the cells in the proximity of the integrated MOFBOTs carrying DOX. Finally, the degradation of the integrated MOFBOT is also shown. While the GelMA core follows an enzymatic degradation process, the degradation of Fe@ZIF-8 involves pH-triggered dissolution of the framework and oxidation of the magnetic components. The presented integrated MOFBOT brings together several features required for biomedical magnetic microrobots. Its magnetic properties stem from magnetic oxide components that could degrade in physiological conditions, instead of rigid magnetic materials such as Ni and Co, which are either passivated and bioaccumulated, and known to cause cytotoxicity, thus requiring retrieval operations. The drug loading was achieved in the MOF crystals, and the release occurred only in acidic pH after MOF degradation, resulting in a local effect once the MOFBOT has reached the target area. The core of the MOFBOT consists of a biodegradable polymer combining the advantages of direct laser writing and shape control, as well as biodegradation in cell cultures. Overall, the combination of the degradable magnetic MOF composites with the gelatin-based chassis results in an unprecedented highly integrated small-scale robot.

4. Experimental Section

Synthesis of MOF composite and fabrication of MOFBOTs. All chemicals were purchased from Sigma-Aldrich. ZIF-8 particles were prepared via a water-based synthesis. Reactant solutions of 5 ml $Zn(OAc)_2 \cdot 2H_2O$ (0.55 M) [383058, Sigma-Aldrich] in deionized (DI) water and 5 ml of 2-Methylimidazole (5.5 M) [M50850, Sigma-Aldrich] in DI water were mixed and homogenized by vortexing for a few seconds. The reaction took place under mild shaking for 24 hours at room temperature. The ZIF-8 crystals were collected after several washing steps using DI water. Fe@ZIF-8 particles were prepared with the following protocol; 2.5 ml of $FeSO_4 \cdot 7H_2O$ (0.43 M) [215422, Sigma-Aldrich] were mixed with 2.5 ml of $Zn(OAc)_2 \cdot 2H_2O$ (0.55 M). The mixture of the metal salts was then added to 5 ml of 2-methylimidazole in DI water (5.5 M). All solutions were prepared with DI water. DOX@Fe@ZIF-8 particles were fabricated following the same procedure, with the addition of DOX 50 μg/ml [PHR1789, Sigma-Aldrich] in the reactant solution. The reaction took place under mild agitation for 24 hours and at room temperature. The Fe@ZIF-8 and the DOX@Fe@ZIF-8 crystals were collected after several washing steps using DI water. The Nanoscribe system from photonic Professional GT was used for the fabrication of the GelMA core of the MOFBOT. The GelMA precursor solution with a water soluble photoinitiator sodium 3,3'-((((1E,1'E)-(2-oxocyclopentane-1,3-diylidene) bis (methanylylidene))bis(4,1-phenylene)) bis(methylazanediyl)) dipropanoate (P2CK) were prepared as described elsewhere.[20] A drop of the precursor solutions was dropped on to a glass slide where the direct laser writing was performed. The Nanoscribe was equipped with a femtolaser of 780 nm and 80 MHz, and the 63x objective was implemented in our experiment. In accordance with our previous research,[20] a laser power of 95 mW and a scanning speed of 10 mm s^{-1} were selected as optimal for this experiment. After exposure, the GelMA cores were developed in water at 50 ºC for 30 minutes. The microstructures obtained were washed and maintained in a 70% ethanol solution. For the integrated MOFBOT, GelMA cores were decorated with Fe@ZIF-8 crystals in a 20 mg/ml water dispersion.

Compositional, morphological and structural characterization. Scanning electron microscopy (SEM) images were recorded with SEM (Zeiss ULTRA 55 plus) operating at 5kV. A drop of water dispersion of the sample was cast on Si chips that had previously been cleaned in acetone, isopropanol and DI water. Once the water had evaporated, the samples were sputtered with a thin layer of Au and the imaging was performed. An OXFORD instruments EDX detector was implemented for spot EDX and EDX mapping analysis. Transmission electron microscopy (TEM), scanning transmission electron microscopy (STEM) and EDX were performed with FEI Talos F200X (Chem S/TEM) operating at 150 kV. The samples were prepared on carbon coated Cu TEM grids (400 mesh) [1824, Ted Pella]. The crystalline phase was confirmed by X-Ray diffraction (XRD) experiments (Bruker AXS D8 Advance). Rutherford Backscattering Spectroscopy (RBS) measurements were performed at 2 MeV He. RUMP simulations were performed to analyze the obtained data. Elastic Recoil Detection Analysis (ERDA) was performed at 13 MeV ^{127}I. XAS measurements across the Zn and Fe $L_{2,3}$ edges were recorded at the BL29-BOREAS beamline of the ALBA Synchrotron (Barcelona, Spain) at room temperature.

Magnetism Characterization. Magnetization curves at room temperature were recorded with a vibrating sample magnetometer (VSM EZ9, Microsense). The field was scanned from -2 T up to 2 T and back. XMCD at the Zn and Fe $L_{2,3}$-edges with a magnetic field of 5 T were performed at the BOREAS beamline, ALBA synchrotron, in Barcelona. Magnetic manipulation of the integrated MOFBOT was performed with a setup consisting of 3 pairs of orthogonally oriented Helmholtz coils.

BET measurements. The surface area was analyzed based on gas adsorption isotherms. N_2 absorption-desorption curve measurements were recorded at 77 K using an Autosorb-IQAG analyser (Quantachrome). Temperature was controlled by using a liquid nitrogen bath. The samples were previously activated at 373 K and 3mbar over 12 hours.

pH responsive drug release. Buffer solutions of pH 6 were prepared from 0.1 M citrate and 0.2 M sodium phosphate dibasic. Buffer solutions of commercial PBS, pH 7.4, were purchased from Thermo Fisher Scientific (Gibco 10010023). The samples were placed on the shaker for mild mixing for various periods of time. DOX release was recorded with absorbance measurements performed with an excitation wavelength of 488 nm, and emission was recorded at 570 nm [Infinite 200 Pro, Tecan]. At various time periods, the samples were centrifuged at 4000 rpm for 3 minutes, and 100 µl of supernatant were collected for the absorbance measurements.

Cell culture experiments. Human breast cancer cells (MDA-MB-231) were cultivated in DMEM cell culture medium [31966021, Thermo Fisher Scientific] (10% fetal bovine serum (FBS) [10270106, Thermo Fisher Scientific], 1 x Antibiotics-Antimycoticum [15240062, Thermo Fisher Scientific]) at physiological conditions (37 °C and 5% CO_2). In vitro DOX delivery experiments were performed in 24-multi well plates. 15,000 cells were seeded in each well 24 hours prior to treatment. On the day of the treatment, the zero-time point, Fe@ZIF-8 crystals and DOX@Fe@ZIF-8 were added to the cell cultures at a concentration of 0.05 mg/ml. The cell viability percentage was calculated based on MTT viability assay 24 and 72 hours after the treatment. For the MTT assay, 50 µl of MTT reagent, 3mg ml^{-1} of 3-(4,5-dimethylthiazol-2-yl)-2,5-diphenyl tetrazolium bromide [M5655, Sigma-Aldrich] in PBS at pH 7.4, was added to each well. The cells were incubated for 4 hours, during this time cells with an active metabolism converted the MTT reagent to a purple colored formazan crystal. The crystals were dissolved in a 0.04 M HCl solution, resulting in a purple colored solution. Finally, the absorbance was measured on a plate reader with a test wavelength of 570 nm and a reference wavelength of 630 nm. For the particle degradation experiments, human embryonic kidney (HEK - 293) cells were cultivated in a DMEM cell culture medium (10% FBS, 1 x Antibiotics-Antimycoticum) at physiological conditions (37 °C and 5% CO_2). Fe@ZIF-8 crystals were introduced at a concentration of 0.05 mg/ml. After one day (24 hour time point), the whole

content of one flask was transported to either a T-25 flask and incubated for one more day (48 hour time point), or to a T-75 flask and incubated for another two days (72 hour time point), or to a T-150 flask and incubated for another three days (96 hour time point). In all cases, the cell cultures were confluent at the time period of interest. Therefore, as indicated in the image for later time periods such as the 120 hour time point, an extra transfer was performed in a 1:4 ratio. The same steps as described above were also performed with control cell cultures (without Fe@ZIF-8 crystals), and the magnetization curves were measured and subtracted, as a background, from the cell cultures with Fe@ZIF-8 crystals. SH-SY5Y cells were cultivated in a mixture of 45 % DMEM cell culture medium, 45% MEM cell culture medium, 10% FBS, 1 x Antibiotics-Antimycoticum. The cells were seeded onto Fe@ZIF-8@GelMA microrobots and the cell cultures were maintained for 2 weeks.

Cell Imaging. Bright field and fluorescence images were obtained using an inverted optical microscope (Olympus IX-81). Confocal microscopy images and stacks were recorded with confocal Microscope Zeiss LSM 780. LIVE/DEAD cell staining was performed according to the protocol from Thermo Fisher Scientific, R37601. Nuclear staining was realized with Hoechst 33342, using NucBlue Live ready Probes Reagent R37605 from Thermo Fisher Scientific. Cell fixation and permeation was performed in a 4% paraformaldehyde 0.01% Triton-X solution. Cytoskeleton staining was performed with phalloidin-tetramethylrhodamine B isothiocyanate [P1951, Sigma-Aldrich].

Statistical Analysis: The particle size of ZIF-8 and Fe@ZIF-8 were calculated based on LogNormal fits of the particle size distributions presented in Figure S1. Sample size n_1=250 and n_2=200 for ZIF-8 and Fe@ZIF-8 respectively. All biological experiments were performed in triplicates. In the figures, the column heights correspond to the average value and the error bars to the standard deviation.

Supporting Information

Supporting Information Biodegradable MOFBOTs

Supporting video 1

Supporting video 2

Acknowledgements

The work presented here was partially financed by the European Research Council Starting Grant microCrysFact (ERC-2015-STG No. 677020), Consolidator Grant "Highly Integrated Nanoscale Robots for Targeted Delivery to the Central Nervous System" HINBOTS under the grant no. 771565, ETH Grant Mofbots (No.ETH-33 17-1) and the Swiss National Science Foundation (Project No.200021_181988). The authors would like to thank Lydia Zehnder from the Institute for Geochemistry and Petrology at ETH for her support on XRD measurements, Dr. Max Doebeli from the Institute for Particle Physics and Astrophysics at ETH for his contribution with the RBS and ERDA measurements, and Prof. Dr. F.M.F. (Frank) de Groot from the University of Utrecht for his advice on the interpretation of XAS measurements. We would also like to acknowledge partial financial support from the 2017-SGR-292 project (Generalitat de Catalunya) and the MAT2017-86357-C3-1-R project (and associated Feder) from the Spanish Government. The XAS and XMCD experiments were performed at the BOREAS beam line at ALBA Synchrotron with the collaboration of ALBA staff. The authors would also like to thank the Scientific Center for Optical and Electron Microscopy (ScopeM) and FIRST laboratory at ETH for their technical support. M. Palacios-Corella acknowledges financial support from the EU (ERC Advanced Grant SPINMOL), the Spanish MINECO (MAT-2014-56143-R and Unidad de Excelencia Mariá de Maeztu MDM-2015-0538), and the COST Association for the support provided through the COST Action MOLSPIN CA15128. X. Wang acknowledges financial support from the China Scholarship Council (No. 201504910817).

Received: ((will be filled in by the editorial staff))

Revised: ((will be filled in by the editorial staff))

Published online: ((will be filled in by the editorial staff))

References

[1] a) W. Hu, G. Z. Lum, M. Mastrangeli, M. Sitti, Nature 2018, 554, 81; b) X. Z. Chen, B. Jang, D. Ahmed, C. Hu, C. De Marco, M. Hoop, F. Mushtaq, B. J. Nelson, S. Pane, Advanced Materials 2018, 30, e1705061; c) J. J. Abbott, Z. Nagy, F. Beyeler, B. J. Nelson, IEEE Robotics & Automation Magazine 2007, 14, 92.

[2] a) H. Ceylan, J. Giltinan, K. Kozielski, M. Sitti, Lab on a Chip 2017, 17, 1705; b) M. Sitti, H. Ceylan, W. Hu, J. Giltinan, M. Turan, S. Yim, E. Diller, Proceedings of the IEEE 2015, 103, 205; c) X. Hu, B. Lim, S. R. Torati, J. Ding, V. Novosad, M.-Y. Im, V. Reddy, K. Kim, E. Jung, A. I. Shawl, E. Kim, C. Kim, Small 2018, 14, 1800504.

[3] a) S. Palagi, A. G. Mark, S. Y. Reigh, K. Melde, T. Qiu, H. Zeng, C. Parmeggiani, D. Martella, A. Sanchez-Castillo, N. Kapernaum, F. Giesselmann, D. S. Wiersma, E. Lauga, P. Fischer, Nature Materials 2016, 15, 647; b) H.-W. Huang, M. S. Sakar, A. J. Petruska, S. Pané, B. J. Nelson, Nature Communications 2016, 7, 12263; c) H. Shum, Micromachines (Basel) 2019, 10, 65.

[4] a) M. Sitti, D. S. Wiersma, Advanced Materials 2020, n/a, 1906766; b) P. Erkoc, I. C. Yasa, H. Ceylan, O. Yasa, Y. Alapan, M. Sitti, Advanced Therapeutics 2019, 2, 1800064; c) A. Aghakhani, O. Yasa, P. Wrede, M. Sitti, Proceedings of the National Academy of Sciences 2020, 117, 3469.

[5] a) C. Chautems, B. Zeydan, S. Charreyron, G. Chatzipirpiridis, S. Pané, B. J. Nelson, European Journal of Cardio-Thoracic Surgery 2017, 51, 405; b) B. Wang, Y. Zhang, L. Zhang, Quant Imaging Med Surg 2018, 8, 461.

[6] a) P. TirgarBahnamiri, S. Bagheri-Khoulenjani, Medical Hypotheses 2017, 102, 56; b) K. E. Peyer, L. Zhang, B. J. Nelson, Nanoscale 2013, 5, 1259; c) J. Park, C. Jin, S. Lee, J.-Y. Kim, H. Choi, Advanced Healthcare Materials 2019, 8, 1900213.

[7] M. Sitti, Nature Reviews Materials 2018, 3, 74.

[8] A. Terzopoulou, M. Hoop, X.-Z. Chen, A. M. Hirt, M. Charilaou, Y. Shen, F. Mushtaq, A. P. del Pino, C. Logofatu, L. Simonelli, A. J. de Mello, C. J. Doonan, J. Sort, B. J. Nelson, S. Pané, J. Puigmartí-Luis, Angewandte Chemie International Edition 2019, 58, 13550.

[9] a) H. Furukawa, K. E. Cordova, M. O'Keeffe, O. M. Yaghi, Science 2013, 341, 1230444; b) P. Horcajada, T. Chalati, C. Serre, B. Gillet, C. Sebrie, T. Baati, J. F. Eubank, D. Heurtaux, P. Clayette, C. Kreuz, J.-S. Chang, Y. K. Hwang, V. Marsaud, P.-N. Bories, L. Cynober, S. Gil, G. Férey, P. Couvreur, R. Gref, Nature Materials 2010, 9, 172; c) N. Stock, S. Biswas, Chemical Reviews 2012, 112, 933.

[10] a) P. Horcajada, R. Gref, T. Baati, P. K. Allan, G. Maurin, P. Couvreur, G. Férey, R. E. Morris, C. Serre, Chemical Reviews 2012, 112, 1232; b) S. Keskin, S. Kızılel, Industrial & Engineering Chemistry Research 2011, 50, 1799; c) M.-X. Wu, Y.-W. Yang, Advanced Materials 2017, 29, 1606134; d) K. Lu, T. Aung, N. Guo, R. Weichselbaum, W. Lin, Advanced Materials 2018, 30, 1707634.

[11] a) X.-G. Wang, Z.-Y. Dong, H. Cheng, S.-S. Wan, W.-H. Chen, M.-Z. Zou, J.-W. Huo, H.-X. Deng, X.-Z. Zhang, Nanoscale 2015, 7, 16061; b) Q. Wu, M. Li, L. Tan, J. Yu, Z. Chen, L. Su, X. Ren, C. Fu, J. Ren, L. Li, F. Cao, P. Liang, Y. Zhang, X. Meng, Nanoscale Horizons 2018, 3, 606; c) L. Gao, Q. Chen, T. Gong, J. Liu, C. Li, Nanoscale 2019, 11, 21030; d) D. Wang, J. Zhou, R. Shi, H. Wu, R. Chen, B. Duan, G. Xia, P. Xu, H. Wang, S. Zhou, C. Wang, H. Wang, Z. Guo, Q. Chen, Theranostics 2017, 7, 4605.

[12] B. Khezri, M. Pumera, Advanced Materials 2019, 31, 1806530.

[13] a) R. Ricco, L. Malfatti, M. Takahashi, A. J. Hill, P. Falcaro, Journal of Materials Chemistry A 2013, 1, 13033; b) J. Aguilera-Sigalat, D. Bradshaw, Coordination Chemistry

Reviews 2016, 307, 267; c) X. Wang, X.-Z. Chen, C. C. J. Alcântara, S. Sevim, M. Hoop, A. Terzopoulou, C. de Marco, C. Hu, A. J. de Mello, P. Falcaro, S. Furukawa, B. J. Nelson, J. Puigmartí-Luis, S. Pané, Advanced Materials 2019, 31, 1901592.

[14] M. Jian, B. Liu, R. Liu, J. Qu, H. Wang, X. Zhang, RSC Advances 2015, 5, 48433.

[15] A. Barla, J. Nicolas, D. Cocco, S. M. Valvidares, J. Herrero-Martin, P. Gargiani, J. Moldes, C. Ruget, E. Pellegrin, S. Ferrer, Journal of Synchrotron Radiation 2016, 23, 1507.

[16] a) J. P. Singh, B. Kaur, A. Sharma, S. H. Kim, S. Gautam, R. C. Srivastava, N. Goyal, W. C. Lim, H. J. Lin, J. M. Chen, K. Asokan, D. Kanjilal, S. O. Won, I.-J. Lee, K. H. Chae, Physical Chemistry Chemical Physics 2018, 20, 12084; b) D. H. Kim, H. J. Lee, G. Kim, Y. S. Koo, J. H. Jung, H. J. Shin, J. Y. Kim, J. S. Kang, Physical Review B 2009, 79, 033402.

[17] I. Brigger, C. Dubernet, P. Couvreur, Advanced Drug Delivery Reviews 2002, 54, 631.

[18] M. Hoop, C. F. Walde, R. Riccò, F. Mushtaq, A. Terzopoulou, X.-Z. Chen, A. J. deMello, C. J. Doonan, P. Falcaro, B. J. Nelson, J. Puigmartí-Luis, S. Pané, Applied Materials Today 2018, 11, 13.

[19] L. Gu, R. H. Fang, M. J. Sailor, J.-H. Park, ACS nano 2012, 6, 4947.

[20] X. Wang, X.-H. Qin, C. Hu, A. Terzopoulou, X.-Z. Chen, T.-Y. Huang, K. Maniura-Weber, S. Pané, B. J. Nelson, Advanced Functional Materials 2018, 28, 1804107.

[21] F. Qiu, B. J. Nelson, Engineering 2015, 1, 021.

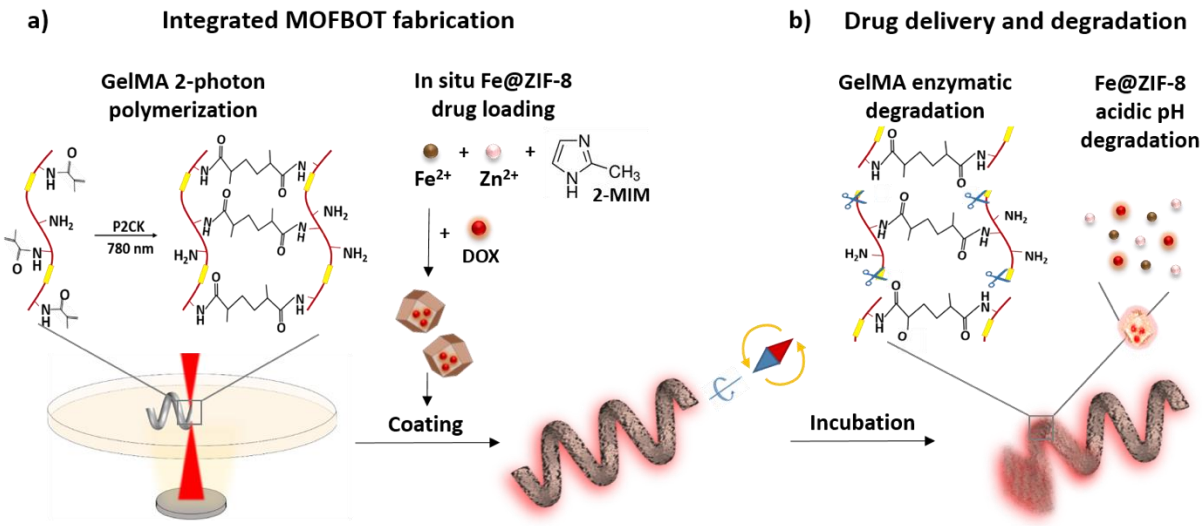

Figure 1. a) Schematic illustration of the fabrication of a MOFBOT. First, the GelMA chassis is fabricated with direct laser writing, using two-photon polymerization (2PP) stereolithography, and subsequently the chassis is decorated with pre-synthesized DOX@Fe@ZIF-8 crystals. b) An illustration of the degradation of the MOFBOT. While the GelMA chassis degrades via enzymatic hydrolysis, Fe@ZIF-8 crystals degrade via an acidic pH-triggered process.

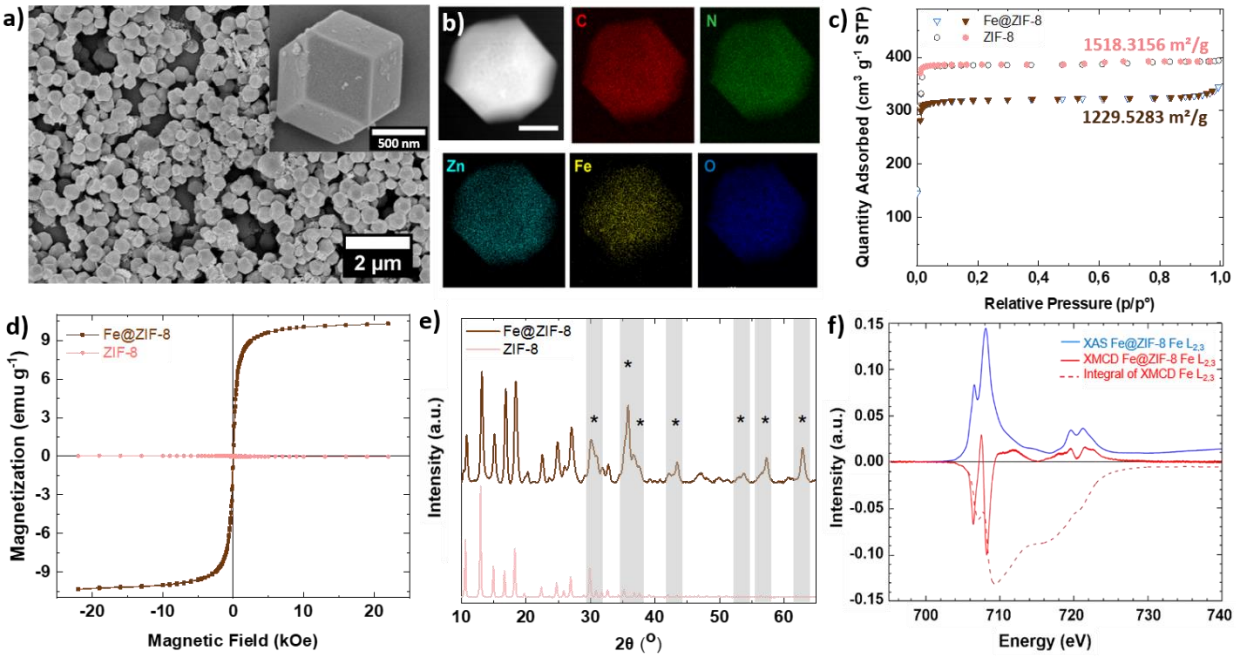

Figure 2. a) SEM images of Fe@ZIF-8. b) High-angle annular dark field (HAADF) and EDX maps of a single Fe@ZIF-8 crystal. The EDX maps show the C, N, Zn, Fe and O distribution in the crystal. The scale bar is 250 nm. c) N_2 absorption-desorption isotherms and calculated BET surface area. d) Magnetization curves of soft magnetic Fe@ZIF-8 and diamagnetic ZIF-8. e) XRD patterns of ZIF-8 and Fe@ZIF-8. The asterisks indicate the extra peaks present in the Fe@ZIF-8 crystals. f) XAS and XMCD spectra (multiplied by a factor 5) of Fe@ZIF-8 at the Fe $L_{2,3}$ edges, and integrated XMCD signal (multiplied by a factor 5) showing convergence to ~zero.

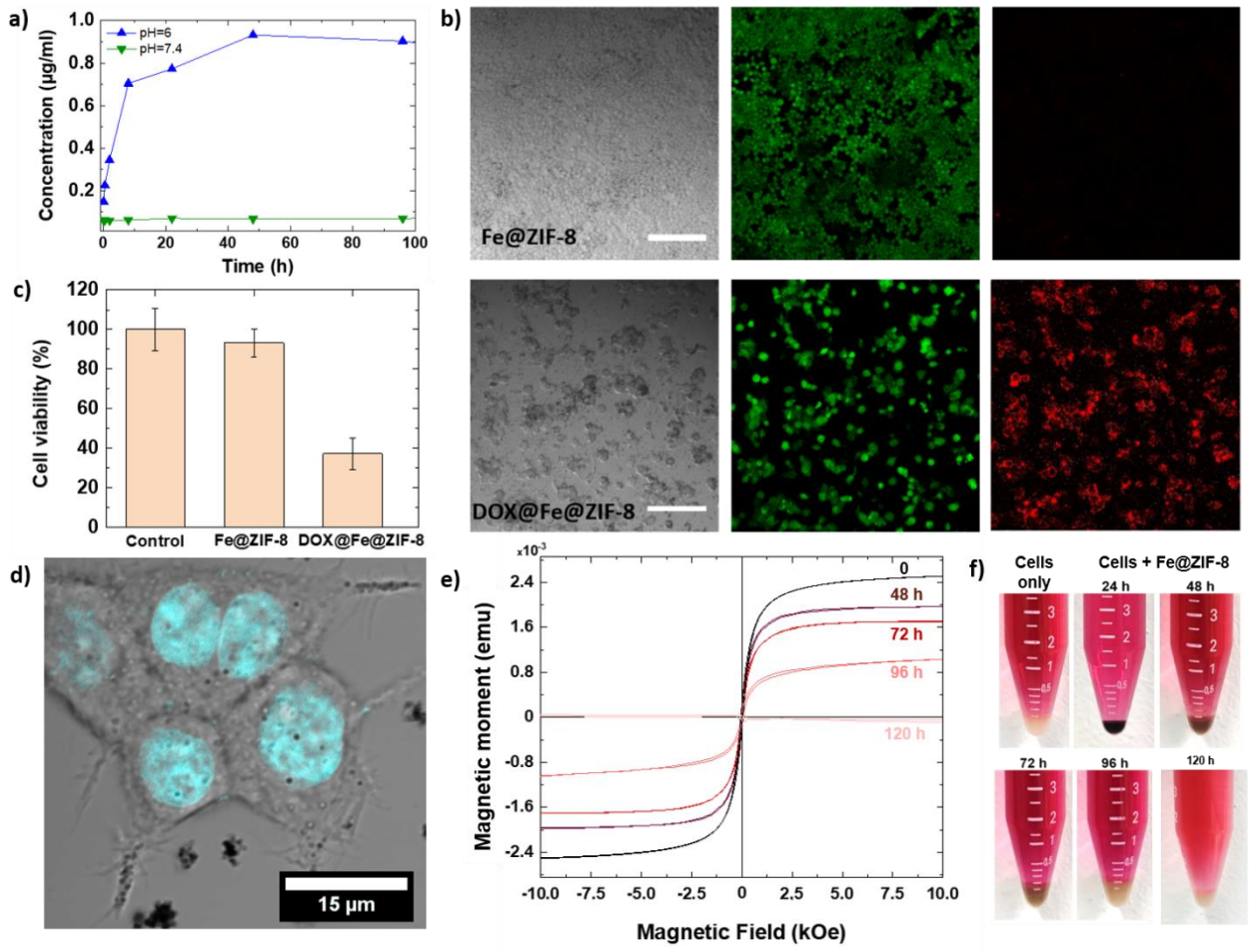

Figure 3. a) DOX release from Fe@ZIF-8 composite particles in buffer solutions at different pH, i.e. pH=6 and pH=7.4. b) LIVE/DEAD staining images of cells incubated with Fe@ZIF-8 and DOX@Fe@ZIF-8, scale bars 200 µm. c) Cell viability analysis for MDA-MB-231 cells showing efficient drug delivery of DOX *in vitro* after 72 hours of treatment. d) Interaction of Fe@ZIF-8 particles with cells in a culture. e) Magnetic moment measurement of the cell pellet showing the change in the magnetic properties over time in a cell culture. f) The color change of cell pellets incubated with Fe@ZIF-8 crystals at different time periods.

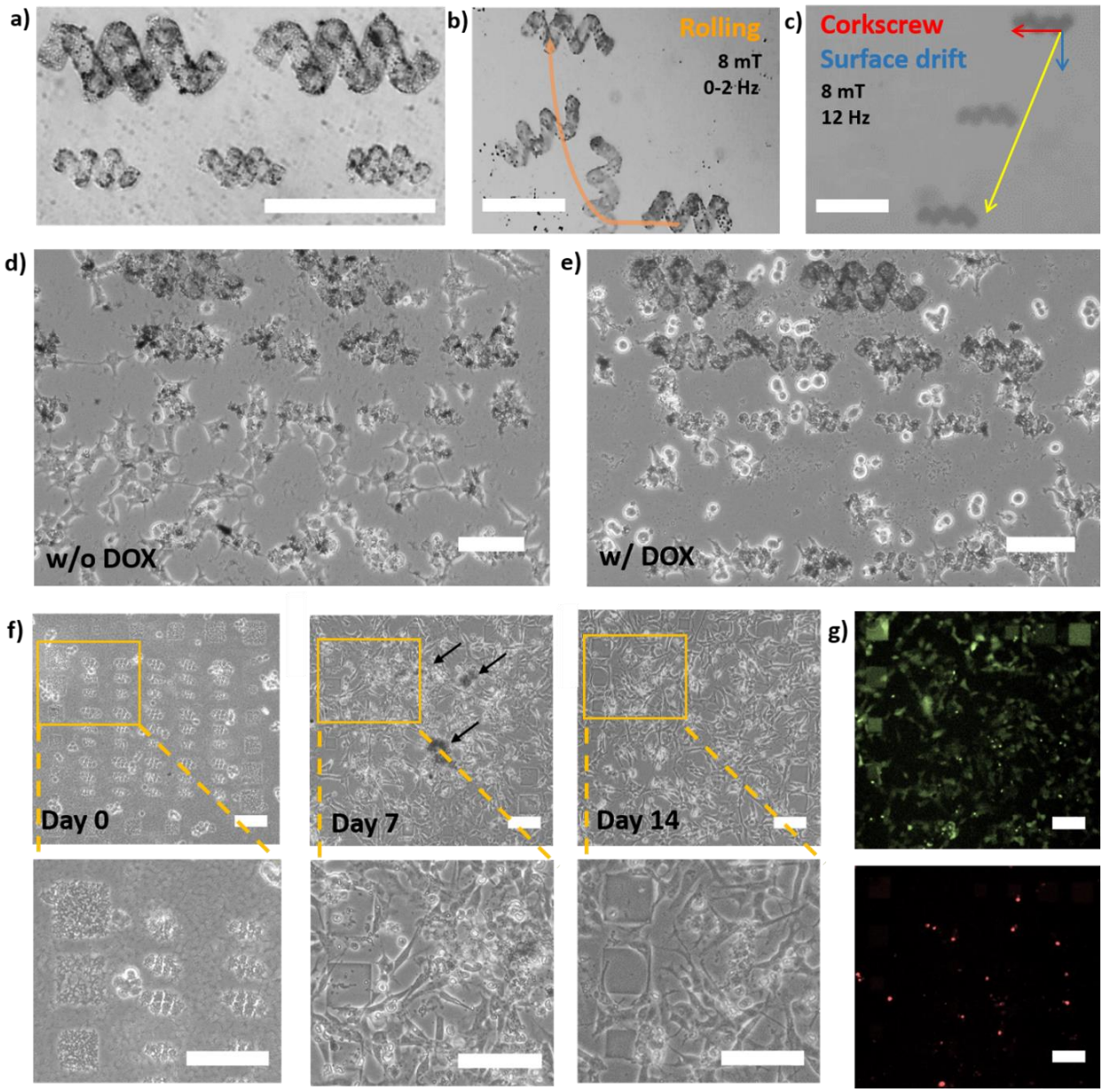

Figure 4. a) Optical microscope images of integrated MOFBOTs. b) and c) Magnetic manipulation of Fe@ZIF-8@GelMA structures with a rotating magnetic field at low and high frequencies showing different locomotion patterns. d) Cells incubated with Fe@ZIF-8@GelMA and e) delivery of DOX with integrated MOFBOTs (DOX@Fe@ZIF-8@GelMA). f) Degradation of the integrated MOFBOT in the cell culture at days 0, 7 and 14. g) LIVE/DEAD staining at the end of the experiments (14 days). The length of the scale bars at a), b), d), e), f) and g) is 100 μm, and 50 μm in c).

Supporting Information

Biodegradable MOFBOTs

Anastasia Terzopoulou, Xiaopu Wang, Xiang-Zhong Chen, Mario Palacios-Corella, Carlos Pujante, Javier Herrero-Martín, Dr. Xiao-Hua Qin, Jordi Sort, Andrew J. deMello, Bradley J. Nelson, Josep Puigmartí-Luis*, and Salvador Pané*

Table of Content

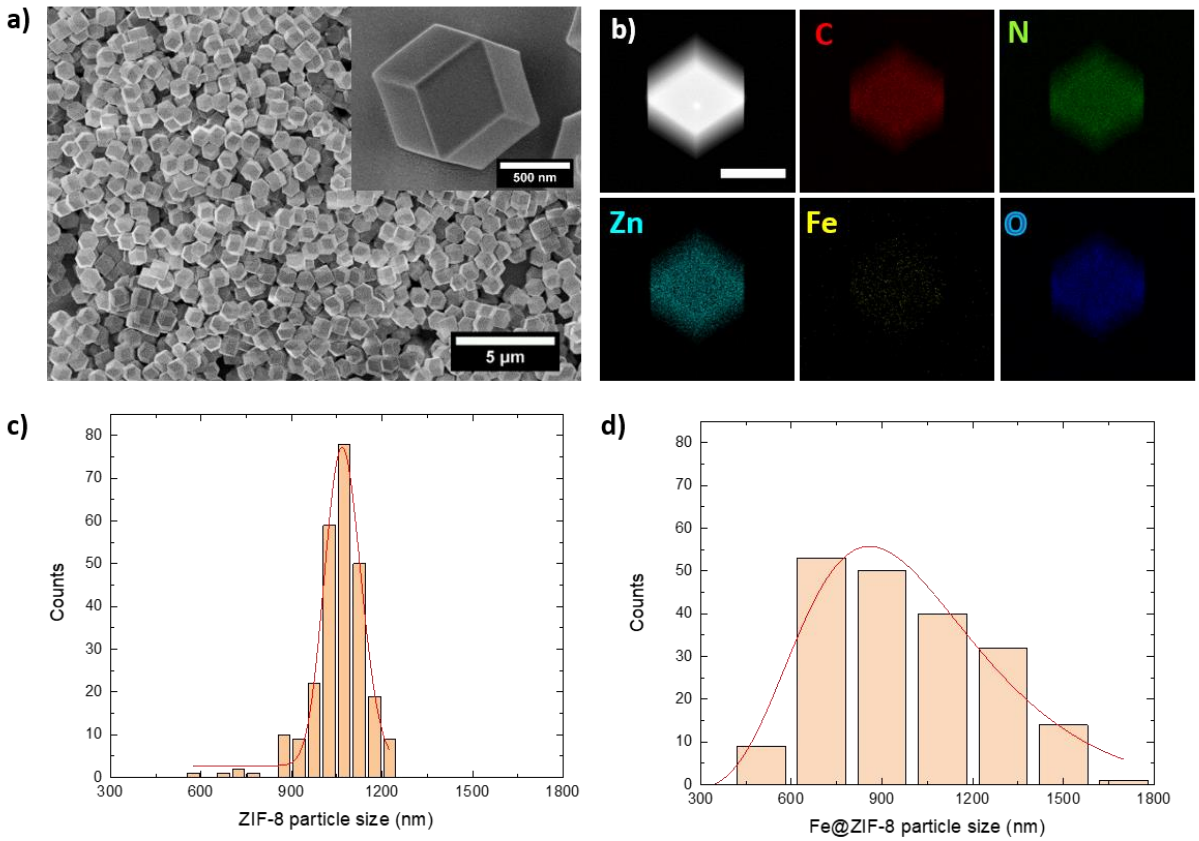

Figure S1. a) SEM images of ZIF-8 showing the dodecahedral shape of the MOF. b) HAADF image and EDX maps of one single ZIF-8 particle, showing the distribution of elements C, N, Zn, Fe and O (scale bar 500 nm). c) Size distribution of pristine ZIF-8 MOFs. Sample size n_1=250 d) Size distribution of Fe@ZIF-8 MOF composites. Sample size n_2=200.

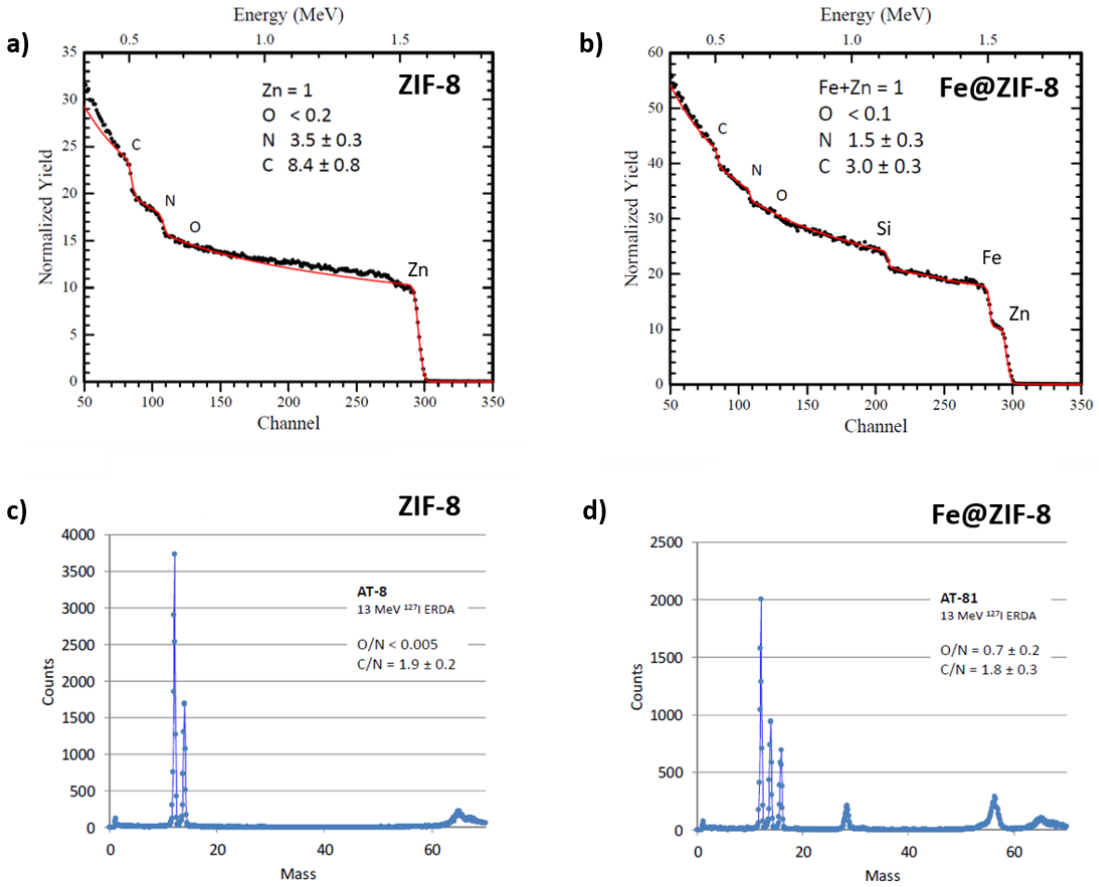

Figure S2. a) and b) RBS measurements and RUMP simulations for ZIF-8 and Fe@ZIF-8 respectively. RBS measurement data shown with black dots and RUMP simulations in red lines allowing for quantification of the elements. The presence of Zn for ZIF-8 and the theoretical ratios from the chemical formula $C_8H_{10}N_4Zn$ were verified. The presence of Zn and Fe for Fe@ZIF-8 is indicated along with an excess of these metals compared to ZIF-8, regarding carbon and nitrogen content. RBS method is not sensitive to light elements, therefore ERDA was implemented, shown in c) and d). For ZIF-8 the theoretical ratio of C/N ~ 2 was verified, while O was not present (below the detection limit). For Fe@ZIF-8 the presence of oxygen was confirmed, while the theoretical ratio of C/N ~ 2 of the ZIF-8 framework was maintained here. The excess of metals indicated by the RUMP simulations together with the presence of O indicate the presence of a secondary phase.

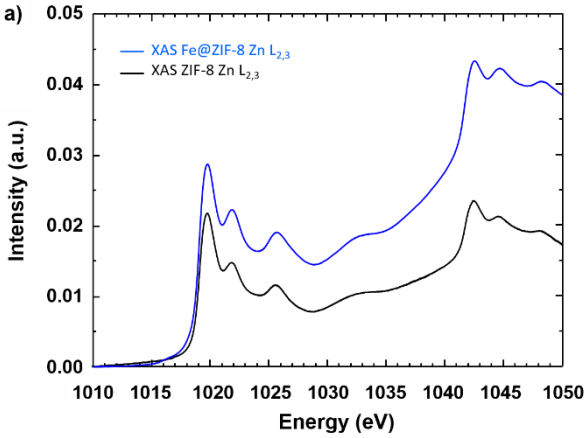

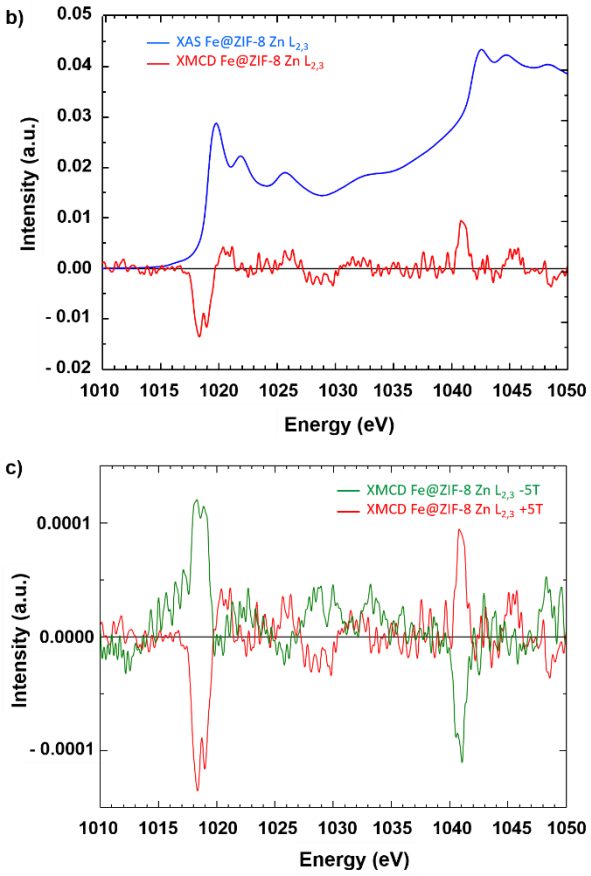

Figure S3. X-ray spectroscopy at the Zn $L_{2,3}$ edges: a) XAS of Fe@ZIF-8 (blue) and ZIF-8 (black); b) Fe@ZIF-8 XAS (blue) and XMCD (red) multiplied by a factor of 100 at +5 T applied; c) Fe@ZIF-8 XMCD as measured for an applied magnetic field of +5 T (red) and -5 T (green) showing that the weak signal detected was of magnetic origin.

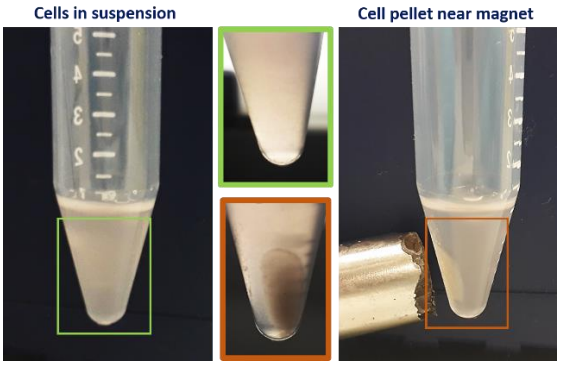

Figure S4. Live cell suspensions after 72 hours incubation with Fe@ZIF-8, showing attraction towards an external magnet and forming a cell pellet near the magnet.

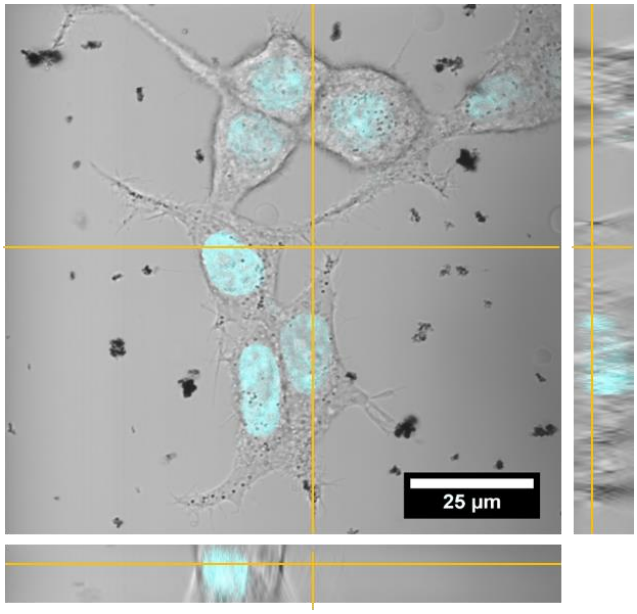

Figure S5. Confocal microscopy images, with Hoechst 33342 nuclear staining, showing interaction of Fe@ZIF-8 particles with cells in culture.

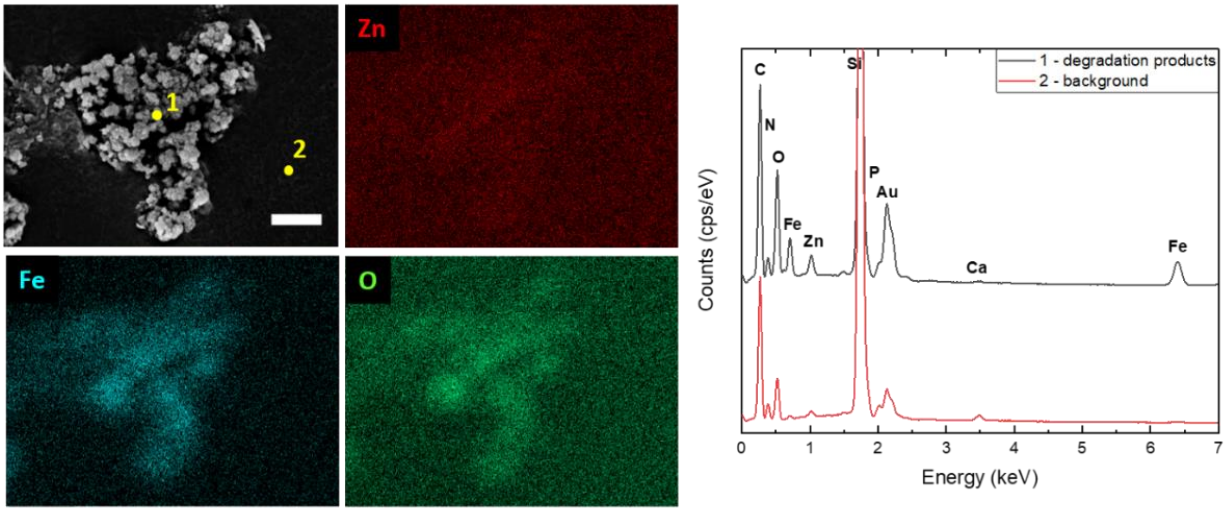

Figure S6. SEM image and EDX mapping of the degradation products after 72 hours incubation of Fe@ZIF-8 in a cell culture (scale bar 500 nm). The EDX spectra show the excess presence of Fe, Zn, and O on the degradation products, compared to the background.

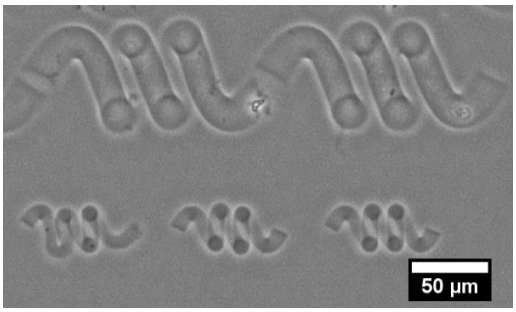

Figure S7. GelMA helical microstructures before incubation with MOF particles.

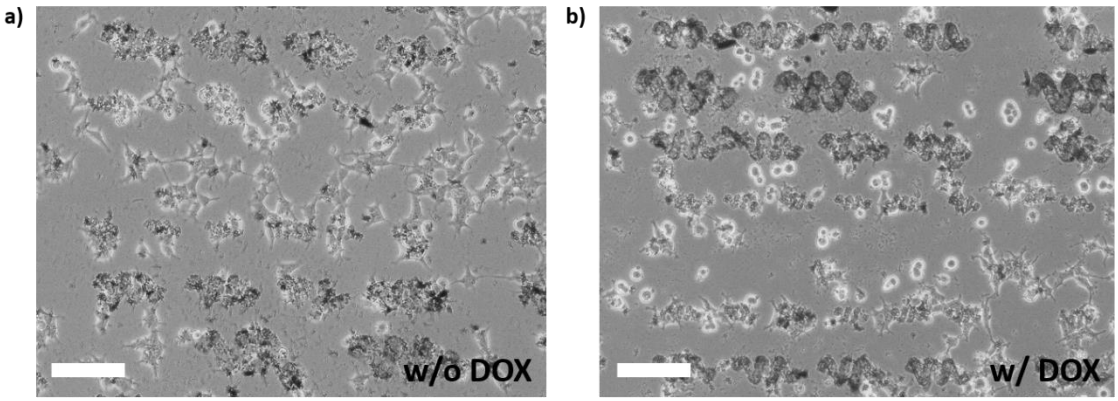

Figure S8. Drug delivery with MOFBOTs to MDA-MB-231 breast cancer cell line *in vitro*. While no obvious toxicity is observed in the case of Fe@ZIF-8 (a), cells in the proximity of the MOFBOTs decorated with DOX@Fe@ZIF-8 appear to be dead (b) (Scale bars: 100 µm).